Hybrid Testing of Wind Turbine Components using Kane's Method

Frederik Nordtorp[a,*], Elif Ecem Baş[b], Cláudio Gomes[c], Per Jensen[d], Jan Jørgensen[e], Giuseppe Abbiati[a]

[a]*Department of Civil and Architectural Engineering, Aarhus University, Inge Lehmanns Gade 10, Aarhus, 8000, Denmark*
[b]*R&D Test Systems A/S, Sigma 3, Hinnerup, 8382, Denmark*
[c]*Department of Electrical and Computer Engineering, Aarhus University, Finlandsgade 22, Aarhus N, 8200, Denmark*
[d]*FORCE Technology, Sandblæservejen 4 , Munkebo, 5330, Denmark*
[e]*FORCE Technology, Park Allé 345, Brøndby, 2605, Denmark*

Abstract

Hybrid testing combines numerical simulations with physical experiments to evaluate large mechanical systems, such as wind turbines, that are impractical to test at full scale. While hybrid testing has been widely applied in structural dynamics, its extension to complex multibody dynamic systems remains challenging due to nonlinear kinematics and strongly coupled degrees of freedom. Although the Kane method underpins widely used wind turbine simulation tools, hybrid testing frameworks that directly integrate Kane-based multibody formulations and interface force coupling remain largely unexplored. Here, a stepwise hybrid testing framework is presented in which the equations of motion are formulated using the Kane method, enabling a systematic treatment of multibody dynamics within hybrid testing. Interface forces are identified from free-body diagrams and incorporated into the equations of motion through the principle of virtual power, allowing consistent coupling between numerical and physical substructures. The framework is demonstrated in a pseudo-dynamic hybrid test of a 13-degree-of-freedom simplified wind turbine rotor system, where a pitch bearing is tested as a physical substructure under force-controlled bi-axial bending and displacement-controlled pitch rotation. A virtual hybrid test validates the formulation and coordination algorithm, while the physical hybrid test demonstrates stable mixed-mode coupling under experimental feedback. The results show that the framework can couple a Kane-based multibody model with a physical wind turbine component and capture its influence on the system-level rotor response.

Keywords:
Hybrid testing, Rotor dynamics, Nonlinear vibration, Wind turbine, Kane method, Pitch bearing, Multibody dynamics

*Corresponding author.
Email address: fnk@cae.au.dk (Frederik Nordtorp)

1. Introduction

1.1. Background and motivation

As wind turbines (WTs) continue to increase in size and capacity, physical testing remains a major bottleneck in the development and validation of new turbine components. For example, accelerated fatigue testing of blades and nacelles may last up to 6–8 months. The community recognizes that some of these tests could be substantially shortened provided that the loading sequence comprehensively captures critical loading scenarios. This has motivated the development of alternative testing methodologies that combine physical testing with numerical simulation.

Hybrid testing (HT) enables testing a physical substructure (PS) of an engineering system while numerically simulating its interaction with the remaining numerical substructure (NS) [1, 2]. The PS and NS are coupled through a control system and servo-controlled actuators, while a coordination algorithm based on numerical time integration or control theory enforces dynamic equilibrium and kinematic compatibility between the two substructures. To address scaling issues and actuation limitations, the wall-clock time associated with testing the PS may be faster than, equal to, or slower than the simulation time. In civil engineering applications, limited actuation capacity typically necessitates testing at speeds slower than real time, requiring the PS to exhibit nearly rate-independent behavior. While HT has been extensively developed for seismic testing of civil engineering structures [3, 4], more recent applications have addressed fire [5], hydrodynamic [6], aerodynamic loading [7], and multi-actuator setups [8, 9, 10]. Consequently, the application of HT to wind turbines is becoming increasingly relevant.

To evaluate the dynamic response of WTs under realistic loading conditions, HT methodologies have been employed in several applications. Sauder *et al.* [11] advocate applying physical hydrodynamic loading on floating substructures within an ocean basin while numerically simulating aerodynamic loading and rotor system dynamics. Similarly, Belloli *et al.* [12] propose applying physical aerodynamic loading on rotor systems in wind tunnels while simulating hydrodynamic loads on floaters. Zhang *et al.* [13] apply HT to evaluate a tuned liquid damper coupled with a numerically simulated 13-DOF wind turbine model. These studies demonstrate the potential of HT for wind turbine applications and motivate the use of system-level models for capturing the coupled mechanical response of interconnected parts.

As WTs are characterized by interconnected parts that undergo large rotations, multibody dynamic (MBD) modeling is essential to accurately capture their dynamic behavior. Among WTs, HT has been applied to various MBD systems, such as biomechanics [14], railway systems [15, 16, 17], vehicle dynamics [18], and robotics [19]. In some of these applications the NS is simulated using software like SIMPACK or FreeDyn, while others formulate the equation of motion from Lagrangian, Hamiltonian, or Newton-Euler methods. Alongside these classical approaches, Kane's method is a well-established formulation in multibody dynamics and has been employed in academic and software-based implementations.

In the context of wind energy, the Kane method underpins the structural dynamics formulation in FAST [20], which is widely used for wind turbine aeroelastic simulation in the research community. Additionally, Sarkar et al. [21] demonstrates the use of the Kane's method in deriving the equations of motion of a floating offshore wind turbine. Introduced

in 1965, the Kane method [22, 23, 24] offers an alternative to classical formulations by deriving the equations of motion directly from the principle of virtual power. It is widely recognized to yield expressions of reduced symbolic complexity and to facilitate formulations with a minimal set of degrees of freedom. These properties avoid the need for additional kinematic constraints and associated differential–algebraic equation (DAE) solvers, which is advantageous for hybrid testing applications. Despite the long-standing development of HT, to the authors' knowledge, HT frameworks that integrate multibody dynamic formulations based on the Kane method remain largely unexplored.

1.2. Scope

In this work, a hybrid testing framework for multibody dynamic systems is presented, in which the equation of motion is formulated using the Kane method and coupled to a physical substructure operating under force-controlled conditions. The framework is first presented through a simple hybrid system and it is then demonstrated experimentally through a hybrid wind turbine rotor model in which one pitch bearing is tested under mixed-mode control.

The paper is organized as follows. Section 1 introduces the background, motivation, and scope. Section 2 presents the hybrid testing framework, including the formulation of the hybrid model for a simplified system and the coordination algorithm for coupling the NS to the PS in force-control. Section 3 demonstrates the framework through a hybrid test of a WT pitch bearing. Section 4 presents and discusses the HT results, and Section 5 concludes the work.

2. Multibody dynamic hybrid testing framework

This section introduces a HT framework formulated for MBD systems. Although the framework applies to systems with multiple interconnected bodies, for clarity, it is illustrated using a simplified single-body example with two degrees of freedom, which serves as a conceptual basis for the wind turbine application presented later in the paper. The hybrid model is shown in Figure 1a, and the testing setup for the PS, as highlighted in red, is illustrated in Figure 1b.

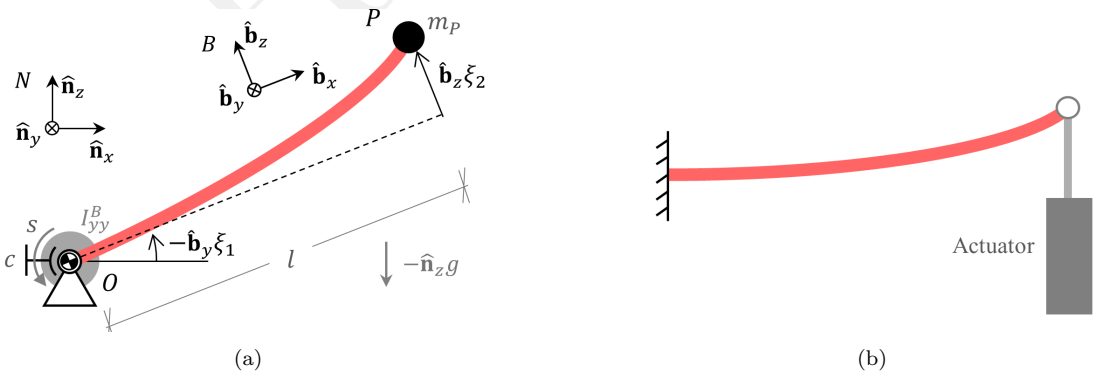

Figure 1: a) Two-degree-of-freedom hybrid model and b) test setup. In both subfigures, the physical substructure is highlighted in red

A cantilever beam serves as the PS, while the remaining components comprise the NS. The first generalized coordinate, ξ_1, describes the rotation of a body attached to frame B_1 about

a fixed point O in the negative $\hat{\mathbf{n}}_y$-direction. The second generalized coordinate, ξ_2, describes the tip displacement of the cantilever beam attached to the body, in the $\hat{\mathbf{b}}_z$-direction. To simplify the model, stress stiffening effects are neglected. The body is rotationally damped with the damping coefficient c and an external torque s is applied in the negative $\hat{\mathbf{b}}_y$-direction. The body attached to B has a mass of inertia I^B_{yy} in its $\hat{\mathbf{b}}_y$-direction. Gravity g acts in the negative $\hat{\mathbf{n}}_z$-direction.

2.1. Formulation of multibody dynamical hybrid model

Following the Kane method as presented by Banerjee [24] and Roithmayr *et al.* [25], a hybrid model is formulated for the simplified system described in the previous section. The symbolic derivation is implemented using the *Mechanics* module of *SymPy* [26, 27], a Python-based library for analytical mechanics.

Rather than presenting a generic derivation of the Kane method, this section illustrates, in a stepwise manner, how the formulation is applied to assemble a hybrid model for the outlined system. The formulation extends and further develops the approach introduced in the authors' earlier conference paper [28]. It proceeds through the definition of (i) reference frame orientations, (ii) position vectors, (iii) inertia forces and torques, (iv) active forces and torques, (v) interface forces and torques, (vi) the principle of virtual power, and (vii) the assembly of the equations of motion.

(i) Reference frame orientations are first defined. The Kane method builds upon a projection of forces and torques to the direction of partial velocities, and all vector quantities (e.g., positions and forces) are reported by explicitly stating the reference frame components. The set of generalized coordinates $\boldsymbol{\xi} = \left[\xi_1, \xi_2\right]^T$ defines the relative orientation between these frames and thus the projection basis. In particular, the orientation of the body-fixed frame B relative to the inertial frame N is described by the rotation matrix,

$$
{}^N\mathbf{C}^B = \begin{bmatrix} \hat{\mathbf{n}}_x \cdot \hat{\mathbf{b}}_x & \hat{\mathbf{n}}_x \cdot \hat{\mathbf{b}}_y & \hat{\mathbf{n}}_x \cdot \hat{\mathbf{b}}_z \\ \hat{\mathbf{n}}_y \cdot \hat{\mathbf{b}}_x & \hat{\mathbf{n}}_y \cdot \hat{\mathbf{b}}_y & \hat{\mathbf{n}}_y \cdot \hat{\mathbf{b}}_z \\ \hat{\mathbf{n}}_z \cdot \hat{\mathbf{b}}_x & \hat{\mathbf{n}}_z \cdot \hat{\mathbf{b}}_y & \hat{\mathbf{n}}_z \cdot \hat{\mathbf{b}}_z \end{bmatrix} = \begin{bmatrix} \cos\xi_1 & 0 & -\sin\xi_1 \\ 0 & 1 & 0 \\ \sin\xi_1 & 0 & \cos\xi_1 \end{bmatrix} \tag{1}
$$

where N denotes the inertial reference frame, defined by the orthonormal unit vectors $\hat{\mathbf{n}}_x$, $\hat{\mathbf{n}}_y$, and $\hat{\mathbf{n}}_z$. The frame B is fixed to the body and described by the local unit vectors $\hat{\mathbf{b}}_x$, $\hat{\mathbf{b}}_y$, and $\hat{\mathbf{b}}_z$.

Angular velocities and accelerations follow directly from the time derivatives of the reference frame orientations. In the present work, these relations are evaluated symbolically using the *Mechanics* module of *SymPy*. This follows from the fact that taking the time derivative in the inertial frame, denoted $\frac{{}^N d}{dt}$, of a unit vector $\hat{\mathbf{b}}_k$ produces a skew-symmetric matrix multiplication. This matrix operation is the equivalent of the vector operation,

$$
\frac{{}^N d}{dt}\hat{\mathbf{b}}_k = \frac{{}^N d}{dt}{}^B\mathbf{C}^N\,{}^N\mathbf{C}^B\hat{\mathbf{b}}_k = {}^N\boldsymbol{\omega}^B \times \hat{\mathbf{b}}_k, \quad k = x, y, z \tag{2}
$$

where $\times$ denotes the cross product, and ${}^N\boldsymbol{\omega}^B$ is the angular velocity of frame B with respect to frame N. This becomes,

$$ {}^N\boldsymbol{\omega}^B = \text{vect}\left(\frac{{}^N d}{dt} {}^B\mathbf{C}^{NN}\mathbf{C}^B \right) = -\dot{\xi}_1 \hat{\mathbf{b}}_y \tag{3} $$

where vect$(\cdot)$ is a vectorization operation following [29]. Deriving the angular velocity in frame N gives the angular acceleration,

$$ {}^N\boldsymbol{\alpha}^B = \frac{{}^N d}{dt} {}^N\boldsymbol{\omega}^B = -\ddot{\xi}_1 \hat{\mathbf{b}}_y \tag{4} $$

(ii) Position vectors are next defined. The generalized coordinates along the directions of the unit vectors define the relative position vector $\mathbf{p}^{OP}$, representing the position of point P with respect to a fixed reference point O,

$$ \mathbf{p}^{OP} = l\hat{\mathbf{b}}_x + \xi_2 \hat{\mathbf{b}}_z \tag{5} $$

where l is the length of the cantilever beam.

Translational velocities and accelerations are automatically derived by the time-derivative in the N frame to the position vectors in (5). By making use of (2), the generic one-point theorem from [26] appears. Accordingly,

$$ {}^N\mathbf{v}^P = \frac{{}^N d}{dt} \mathbf{p}^{OP} = l\dot{\xi}_1 \hat{\mathbf{b}}_z + \dot{\xi}_2 \hat{\mathbf{b}}_z - \xi_2 \dot{\xi}_1 \hat{\mathbf{b}}_x \tag{6} $$

$$ {}^N\mathbf{a}^P = \frac{{}^N d}{dt} {}^N\mathbf{v}^P = l\ddot{\xi}_1 \hat{\mathbf{b}}_z - l\dot{\xi}_1^2 \hat{\mathbf{b}}_x + \ddot{\xi}_2 \hat{\mathbf{b}}_z - 2\dot{\xi}_1 \dot{\xi}_2 \hat{\mathbf{b}}_x - \xi_2 \ddot{\xi}_1 \hat{\mathbf{b}}_x - \xi_2 \dot{\xi}_1^2 \hat{\mathbf{b}}_z \tag{7} $$

(iii) Inertia forces and torques are defined for lumped masses and bodies following the Newton and Euler formulations, respectively. Notably, acceleration from (7), angular velocity from (3), and angular acceleration from (4) are all defined in the inertial frame N. Accordingly,

$$ \mathbf{f}^{*P} = -m_P {}^N\mathbf{a}^P \tag{8} $$

$$ \mathbf{t}^{*B} = -\mathbf{I}^B \cdot {}^N\boldsymbol{\alpha}^B - {}^N\boldsymbol{\omega}^B \times \left(\mathbf{I}^B \cdot {}^N\boldsymbol{\omega}^B \right) \tag{9} $$

where m_P is the mass of the body attached to point P and $\mathbf{I}^B$ is the inertia dyadic of the body attached to frame B. This enables defining the mass of inertia in the principal axis of a given body,

$$ \mathbf{I}^B = I_{yy}^B \hat{\mathbf{b}}_y \otimes \hat{\mathbf{b}}_y \tag{10} $$

where I_{yy}^B is the inertia of the body attached to frame B in its y-direction and $\otimes$ denotes the outer product.

(iv) *Active forces and torques* acting on points and bodies are defined based on the unit vectors from the reference frames.

$$\mathbf{f}^P = -m_P g \hat{\mathbf{n}}_z, \quad \mathbf{t}^B = -s\hat{\mathbf{n}}_y - c\dot{\xi}_1 \hat{\mathbf{n}}_y \tag{11}$$

where s is an external moment and c is a damping coefficient.

(v) *Interface forces and torques* are revealed from a free-body diagram. For the illustrative example, the free-body diagram is presented in Figure 2. The NS is presented in Figure 2a and the PS on the test bench in Figure 2b.

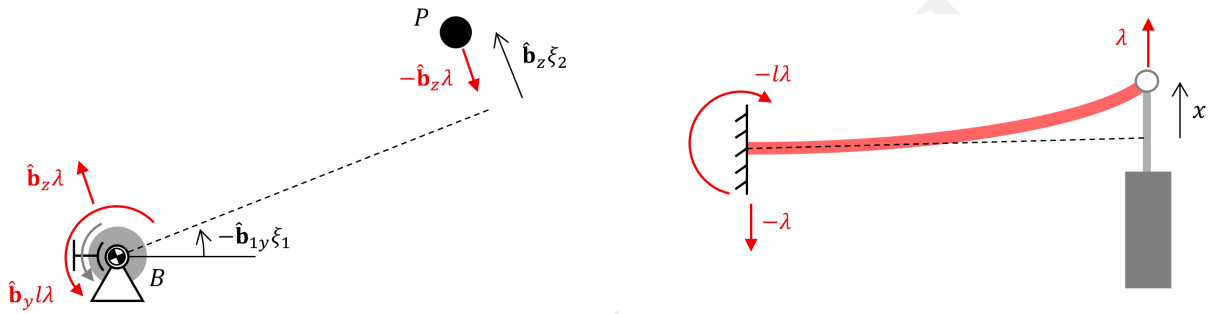

(a) (b)

Figure 2: Free-body-diagram of hybrid structure with interface forces on a) the numerical substructure and b) the physical substructure

In the free-body diagram for the NS, the interface force acting on O and P and the interface torque acting on B read, respectively,

$$\mathbf{f}^{\lambda O} = \lambda \hat{\mathbf{b}}_z, \quad \mathbf{f}^{\lambda P} = -\lambda \hat{\mathbf{b}}_z, \quad \mathbf{t}^{\lambda B} = l\lambda \hat{\mathbf{b}}_y \tag{12}$$

where λ is a Lagrange multiplier constraining the NS to the PS, such that,

$$x = \mathbf{h}\boldsymbol{\xi} \tag{13}$$

where $\mathbf{h} = \begin{bmatrix} 0 & 1 \end{bmatrix}$ is a boolean matrix mapping the degrees-of-freedom of the PS to the NS.

(vi) *The principle of virtual power* is applied following the Kane method. All inertia, active and interface forces are projected onto the partial velocities. As forces on stationary points have no contribution to the virtual power, they can be disregarded. The virtual power associated with $\dot{\xi}_1$ and $\dot{\xi}_2$ sums respectively to,

$$\begin{aligned} F_1 = {}^N\mathbf{v}_1^P \cdot \left(\mathbf{f}^{*P} + \mathbf{f}^P + \mathbf{f}^{\lambda P}\right) + {}^N\boldsymbol{\omega}_1^B \cdot \left(\mathbf{t}^{*B} + \mathbf{t}^B + \mathbf{t}^{\lambda B}\right) = 0 \\ = -c\dot{\xi}_1 + s - gm_P\left(l\cos\xi_1 - \xi_2\sin\xi_1\right) - I_{yy}^B\ddot{\xi}_1 - m_P\left(l^2\ddot{\xi}_1 - l\ddot{\xi}_2 - \xi_2^2\ddot{\xi}_1 - 2\xi_2\dot{\xi}_1\dot{\xi}_2\right) \end{aligned} \tag{14}$$

$$
\begin{aligned}
F_2 = {}^N\mathbf{v}_2^P \cdot \left(\mathbf{f}^{*P} + \mathbf{f}^P + \mathbf{f}^{\lambda P}\right) + {}^N\boldsymbol{\omega}_2^B \cdot \left(\mathbf{t}^{*B} + \mathbf{t}^B + \mathbf{t}^{\lambda B}\right) = 0 \\
= -gm_P \cos\xi_1 - m_P\left(l\ddot{\xi}_1 + \ddot{\xi}_2 - \xi_2\dot{\xi}_1^2\right) - \lambda
\end{aligned}
\tag{15}
$$

where the partial velocities and partial angular velocities are defined with respect to each generalized coordinate derivative. This forms a shared projection basis for the application of virtual power. The generalized velocities of P read,

$$
{}^N\mathbf{v}_1^P = \frac{\partial^N\mathbf{v}^P}{\partial\dot{\xi}_1} = l\hat{\mathbf{b}}_z - \xi_2\hat{\mathbf{b}}_x, \quad {}^N\mathbf{v}_2^P = \frac{\partial^N\mathbf{v}^P}{\partial\dot{\xi}_2} = \hat{\mathbf{b}}_z \tag{16}
$$

and the partial angular velocities of B read,

$$
{}^N\boldsymbol{\omega}_1^B = \frac{\partial^N\boldsymbol{\omega}^B}{\partial\dot{\xi}_1} = -\hat{\mathbf{n}}_y, \quad {}^N\boldsymbol{\omega}_2^B = \frac{\partial^N\boldsymbol{\omega}^B}{\partial\dot{\xi}_2} = \mathbf{0} \tag{17}
$$

(vii) Assembly of the equation of motion (EoM) is done by combining (14) and (15). Accordingly,

$$
\mathbf{M}\ddot{\boldsymbol{\xi}} + \mathbf{f} - \mathbf{h}^T\boldsymbol{\lambda} = \begin{bmatrix} F_1 \\ F_2 \end{bmatrix} = \mathbf{0} \tag{18}
$$

where $\boldsymbol{\lambda} = [\lambda]$ in this example with only one Lagrange multiplier. $\mathbf{M}$ is the mass matrix, whose characteristic for MBD structures is dependent on the state,

$$
\mathbf{M} = \begin{bmatrix} -I_{yy}^B - m_P(l^2 + \xi_2^2) & -m_P l \\ -m_P l & -m_P \end{bmatrix} \tag{19}
$$

Remaining forces composed of external, gravity, Coriolis, and centrifugal force read,

$$
\mathbf{f} = \begin{bmatrix} -c\dot{\xi}_1 + s - gm_P\left(l\cos\xi_1 - \xi_2\sin\xi_1\right) + 2m_P\xi_2\dot{\xi}_1\dot{\xi}_2 \\ -gm_P\cos\xi_1 + m_P\xi_2\dot{\xi}_1^2 \end{bmatrix} \tag{20}
$$

In combination with the set of kinematical equations, this is recast to state space form,

$$
\begin{cases} \dot{\boldsymbol{\xi}} = \mathbf{u} \\ \dot{\mathbf{u}} = -\mathbf{M}^{-1}(\mathbf{f} - \mathbf{h}^T\boldsymbol{\lambda}) \end{cases} \tag{21}
$$

where $\mathbf{u} = \begin{bmatrix} u_1 & u_2 \end{bmatrix}^T$ is a collection of generalized speeds.

The set of differential equations in (21), formulated using Kane's method, provides the basis for the coordination algorithm for the HT.

2.2. Coordination algorithm

In this study, HT is performed in force-control mode by using the coordination algorithm presented in [30]. A coordination algorithm, which may take the form of either a time-integration or control scheme, ensures that the NS and PS satisfy equilibrium and kinematic compatibility. The equation of motion of the hybrid model is described by the following differential algebraic equation (DAE),

$$\begin{cases} \dot{\boldsymbol{\xi}} = \mathbf{u} \\ \dot{\mathbf{u}} = -\mathbf{M}^{-1}(\mathbf{f} - \mathbf{h}^T \boldsymbol{\lambda}) \\ \mathbf{h}\boldsymbol{\xi} - \mathbf{x} = \mathbf{0} \end{cases} \tag{22}$$

Equation (22) is a Hessenberg index-2 DAE, which is solved using the *Baumgarte stabilization* method [31]. Accordingly, interface forces are computed as,

$$\boldsymbol{\lambda} = \left(\mathbf{h}\mathbf{M}^{-1}\mathbf{h}^T\right)^{-1} \left(\mathbf{h}\mathbf{M}^{-1}\mathbf{f} + \ddot{\mathbf{x}} - 2\gamma\left(\mathbf{h}\mathbf{u} - \dot{\mathbf{x}}\right) - \gamma^2\left(\mathbf{h}\boldsymbol{\xi} - \mathbf{x}\right)\right) \tag{23}$$

where $\dot{\mathbf{x}}$ and $\ddot{\mathbf{x}}$ are obtained by polynomial interpolation of the PS kinematic response over the last three time steps. The parameter γ is the Baumgarte stabilization parameter. In this work, the two Baumgarte parameters are set equal, such that $\gamma = \alpha = \beta$, as suggested in [31].

3. Wind turbine case study

This case study demonstrates the proposed hybrid testing framework for testing a WT pitch bearing. Pitch bearings play a central role in load transfer between blades and hub and they have been reported to account for 20% of turbine downtime [32]. Its boundary conditions can be replicated using MAST setups, which apply controlled six-degree-of-freedom (6-DOFs) loading [33, 34, 35], or through blade-bearing-hub tests that reproduce the hub-blade interface using lever arms [36, 37, 38].

Stamler *et al.* [39] concludes that dynamic loads, oscillating movements, and complex interfaces form a set of requirements unique to pitch bearings and identifies that development of new approaches for interface emulations is needed. While component-level testing allows investigation of critical elements, accurately replicating the interaction between components and capturing the full system dynamics remains challenging.

In the present study, the pitch bearing is selected as the PS and is subjected to bi-axial bending, applied in force-control mode, and pitch rotation, applied in displacement-control mode. Force-control is employed for the bending degrees of freedom because the pitch bearing is a stiff component, for which displacement-controlled testing can be adversely affected by actuator compliance and measurement noise.

Section 3.1 presents the hybrid model and Section 3.2 presents the experimental setup.

3.1. Hybrid model

In a 13-DOF hybrid MBD model of a simplified wind turbine rotor system, one pitch bearing is represented as a 3-DOF PS, while the remaining components are described by the

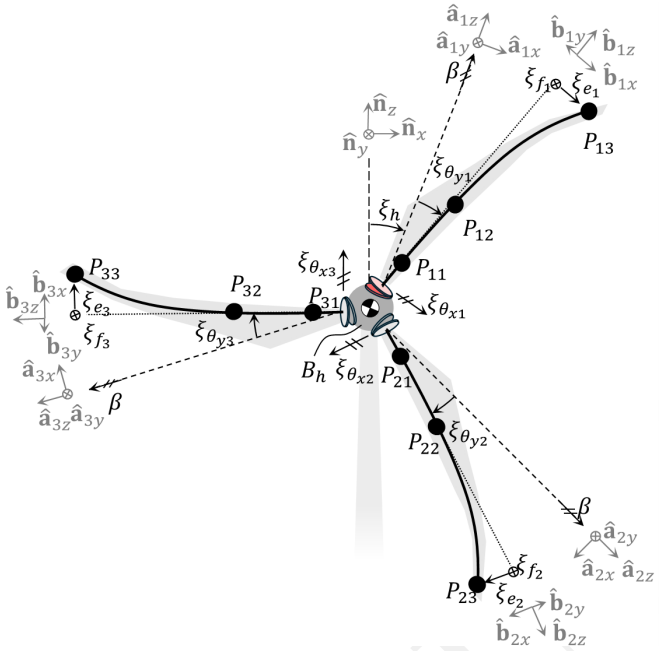

Figure 3: 13-DOF multi-body dynamic hybrid model of a simplified wind turbine rotor, where the pitch bearing represented as the physical substructure is highlighted in red.

NS. An illustration of the hybrid model is presented in Figure 3, where the PS is highlighted in red.

The equation of motion of the hybrid model is associated with 13 DOFs,

$$\boldsymbol{\xi} = \begin{bmatrix} \xi_h & \xi_{\theta_{x1}} & \xi_{\theta_{x2}} & \xi_{\theta_{x3}} & \xi_{\theta_{y1}} & \xi_{\theta_{y2}} & \xi_{\theta_{y3}} & \xi_{e1} & \xi_{e2} & \xi_{e3} & \xi_{f1} & \xi_{f2} & \xi_{f3} \end{bmatrix}^T \tag{24}$$

where the pitch angle β is a time-varying simulation parameter. The model includes a hub, denoted by body B_h, whose rotation is described by the generalized coordinate ξ_h. Three pitch bearings are attached to the hub. Each is associated with a reference frame A_i, oriented according to its azimuth angle and rotated with a pitch angle β along $\hat{\mathbf{a}}_{iz}$. For the i^{th} pitch bearing, the corresponding blade is positioned within the frame B_i. The bending of the pitch bearing is described by two generalized coordinates, $\xi_{\theta_{ix}}$ and $\xi_{\theta_{iy}}$ along the new $\hat{\mathbf{a}}_{ix}$ and $\hat{\mathbf{a}}_{iy}$ directions, respectively. Within each blade, three lumped masses are distributed, and the generalized coordinates describe the displacement of the blade tip ξ_{ei} in the edge-wise and ξ_{fi} in the flap-wise direction, along $\hat{\mathbf{b}}_{ix}$ and $\hat{\mathbf{b}}_{iy}$, respectively. Constant lift and drag forces are applied to the blade tips, and a rotational dashpot represents the generator. The formulation of the EoM follows the framework presented in Section 2.1. The specific formulation and a list of model parameters is provided in Appendix A.

An essential aspect of the hybrid model is the treatment of the interface forces, which are obtained from free-body diagrams and incorporated into the principle of virtual power. The interface forces acting on the NS are shown in Figure 4a, while those on the PS are shown in Figure 4b.

The interface forces are applied as torques to the bodies on either side of the pitch bearing, namely the bodies associated with frames A_1 and B_1. These torques are therefore expressed as,

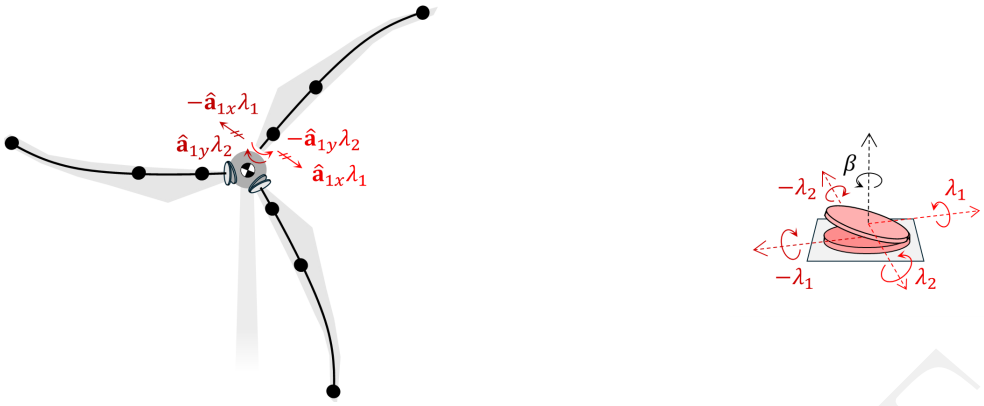

(a) (b)

Figure 4: Free-body-diagram of hybrid structure with interface forces on a) the numerical substructure and b) the physical substructure

$$\mathbf{t}^{\lambda A_1} = \lambda_1 \hat{\mathbf{a}}_{1x} + \lambda_2 \hat{\mathbf{a}}_{1y} \tag{25}$$

$$\mathbf{t}^{\lambda B_1} = -\lambda_1 \hat{\mathbf{a}}_{1x} - \lambda_2 \hat{\mathbf{a}}_{1y} \tag{26}$$

where λ_1 and λ_2 are the bending moments acting on the pitch bearing in the x- and y-directions, respectively. These are defined in the frame rotated by the pitch angle β.

3.2. Experimental setup

The experimental setup has been developed for the purpose of validating the proposed methodology while coping with the limited budget for experimental work. Therefore, the WT case study was conceived around an available SKF slewing bearing with external gears (SLB 061.20.0644), which is used as the PS. Figure 5 shows the experimental test bench at Force Technology in Munkebo, Denmark.

As can be seen in Figure 3, a loading system consisting of a 2 m steel pipe structure converts actuator force/displacement to the boundary conditions applied to the PS. Specifically, Actuators #1 and #2 (250 kN force capacity), which operate in force-control mode, apply bending loads to the PS whereas Actuator #3 (125 kN force capacity), which operates in displacement control-mode imposes the pitch angle. All actuators are equipped with load cells, position sensors, and pressure transducers to enable precise measurement and control throughout the test.

The control system of the experimental setup converts the PS DOFs, which coincide with the task space control variables, to the joint space and vice versa. The latter are the control variables (i.e., force or displacement) associated with each single actuator connected to the loading system. The geometrical transformations between task and joint space coordinates are formulated following [40]. A schematic overview of the complete HT setup is shown in Figure 6.

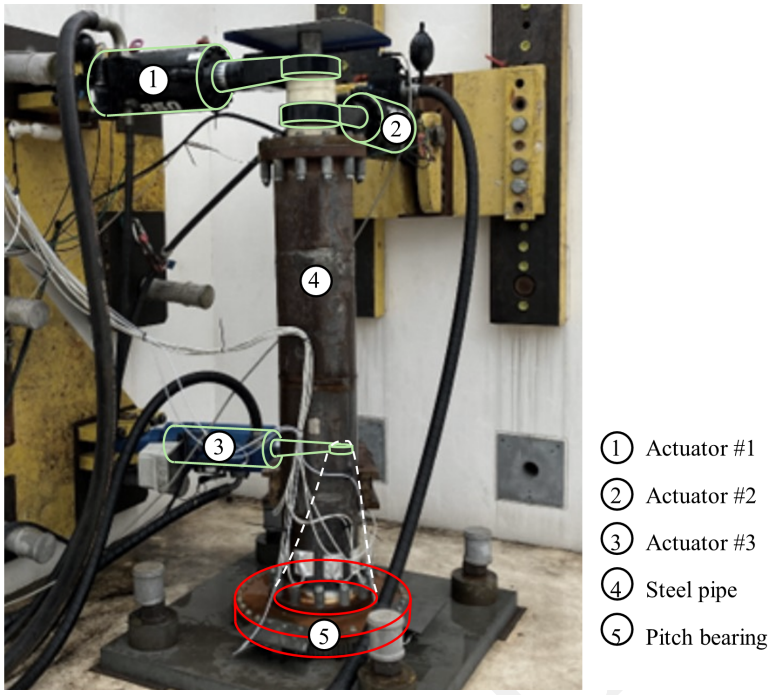

Figure 5: Experimental setup with physical substructure highlighted in red and actuators in green

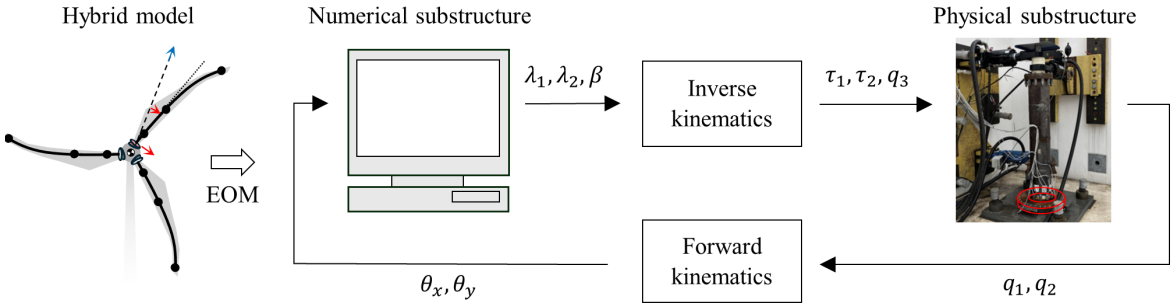

Figure 6: Schematic overview of hybrid test

The TASK-SPACE coordinates $\mathbf{x}$ represent the DOFs from the hybrid model, and TASK-SPACE forces $\mathbf{F}$ represent the interface forces. Accordingly,

$$\mathbf{x} = \begin{bmatrix} \theta_x \\ \theta_y \\ \beta \end{bmatrix}, \quad \mathbf{F} = \begin{bmatrix} \lambda_1 \\ \lambda_2 \\ 0 \end{bmatrix} \tag{27}$$

where θ_x and θ_y are bending angles in x and y-direction and β is a pitch angle in the z direction applied to the bearing. λ_1 and λ_2 are the resulting bending moments in x- and y-direction, respectively. No torque is applied about the pitch axis in force-control mode.

Similarly, the JOINT-SPACE coordinates $\mathbf{q}$ and forces $\boldsymbol{\tau}$ are represented by the actuation system,

$$\mathbf{q} = \begin{bmatrix} q_1 \\ q_2 \\ q_3 \end{bmatrix}, \quad \boldsymbol{\tau} = \begin{bmatrix} \tau_1 \\ \tau_2 \\ 0 \end{bmatrix} \tag{28}$$

where q_1, q_2 and q_3 are actuator elongations. τ_1 and τ_2 are actuator forces.

The *inverse kinematic* associated with the control system is obtained analytically and reads,

$$\mathbf{q} = \mathbf{g}(\mathbf{x}) \tag{29}$$

The *forward kinematics* solution is obtained by solving the following nonlinear algebraic equation using Newton-Raphson,

$$\mathbf{x} = \mathbf{g}^{-1}(\mathbf{q}) \tag{30}$$

The corresponding relation of forces between TASK-SPACE and JOINT-SPACE reads,

$$\mathbf{F} = \mathbf{J}^T \boldsymbol{\tau} \tag{31}$$

$$\boldsymbol{\tau} = \mathbf{J}^{-T} \mathbf{F} \tag{32}$$

where $\mathbf{J}$ represents the Jacobian matrix,

$$\mathbf{J} = \frac{\partial \mathbf{g}(\mathbf{x})}{\partial \mathbf{x}} \tag{33}$$

The tests are performed in a pseudo-dynamic regime, where the hybrid model is advanced in time while the PS is allowed to reach quasi-static equilibrium at each time step. The numerical integration is performed with a time step of 10 ms, while actuator target updates are issued at a lower rate of 0.3 Hz to ensure quasi-static conditions on the test bench.

The coordination procedure follows four main steps:

1. The actuator feedback is converted into pitch bearing bending angles using the forward kinematic relationship.

2. Based on the feedback of the bending angle, the coordination algorithm evaluates the NS and generates the bending moment for the PS, following the procedure outlined in Section 2.2.

3. The commands are transformed into actuator forces and elongations through the inverse kinematic transformation.

4. The resulting actuation commands are sent to the experimental setup, where they are applied by a force-controlled PID control system. Once steady-state conditions are reached on the test bench, the measured actuator elongations are returned to the coordination algorithm, closing the loop and providing updated input for the NS.

Analogously to the implementation of Kane's method, the geometric transformation of the control system is obtained using the *Mechanics* module of *SymPy* [26]. A 2D top-down view of the test bench is presented in Figure 7a, and Figure 7b presents it in a 3D view.

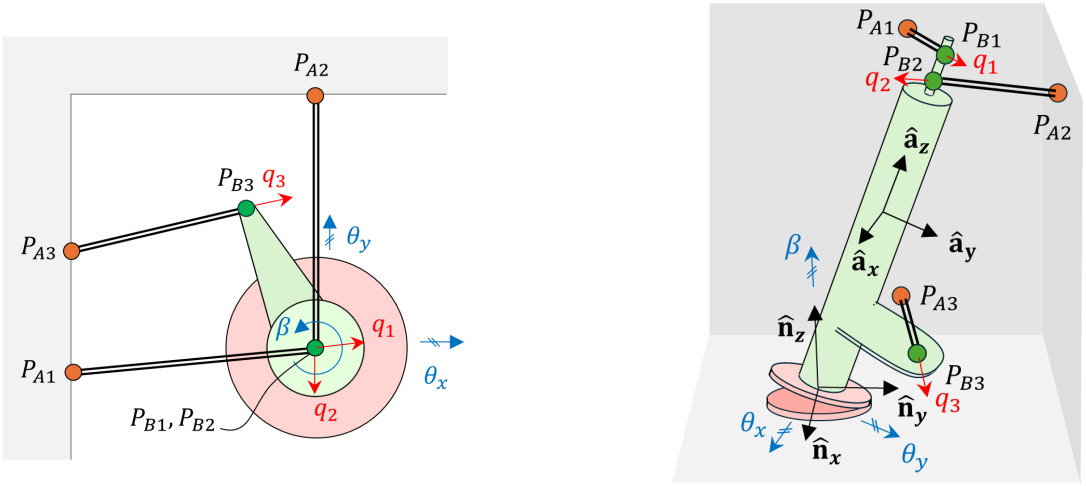

(a) (b)

Figure 7: Sketch of test bench in a) 2D top-down view, and b) 3D view

To describe the positions of the end-effectors in a deformed configuration, a reference frame is attached to the pipe. This frame adopts a partially body-fixed orientation. Initially, the frame undergoes a pitch rotation β about the $\hat{\mathbf{n}}_z$ axis. Subsequently, bending rotations θ_y and θ_x are applied about the rotated axes $\hat{\mathbf{a}}_y$ and $\hat{\mathbf{a}}_x$, respectively. The resulting orientation of frame A relative to frame N is described by the rotation matrix,

$$
{}^{N}\mathbf{C}^{A} = \begin{bmatrix} c_\beta c_{\theta_y} & s_\beta c_{\theta_y} & -s_{\theta_y} \\ -s_\beta c_{\theta_x} + s_{\theta_x} s_{\theta_y} c_\beta & s_\beta s_{\theta_x} s_{\theta_y} + c_\beta c_{\theta_x} & s_{\theta_x} c_{\theta_y} \\ s_\beta s_{\theta_x} + s_{\theta_y} c_\beta c_{\theta_x} & s_\beta s_{\theta_y} c_{\theta_x} - s_{\theta_x} c_\beta & c_{\theta_x} c_{\theta_y} \end{bmatrix} \tag{34}
$$

where $s_{(\cdot)} = \sin(\cdot)$ and $c_{(\cdot)} = \cos(\cdot)$. For each actuator, vectors are defined from the fixed end P_{Ai} to the moving end P_{Bi},

$$
{}^{N}\mathbf{p}^{P_{Ai}P_{Bi}} = P_{Bix}\hat{\mathbf{a}}_x + P_{Biy}\hat{\mathbf{a}}_y + P_{Biz}\hat{\mathbf{a}}_z - (P_{Aix}\hat{\mathbf{n}}_x + P_{Aiy}\hat{\mathbf{n}}_y + P_{Aiz}\hat{\mathbf{n}}_z), \quad (i = 1, 2, 3) \tag{35}
$$

where $(P_{Aix}, P_{Aiy}, P_{Aiz})$ and $(P_{Bix}, P_{Biy}, P_{Biz})$ represent the coordinates of the fixed and moving ends, respectively, for the i-th actuator. The elongation of each actuator is described,

$$
g_i(\mathbf{x}) = \|{}^{N}\mathbf{p}^{P_{Ai}P_{Bi}}\| - l_i, \quad (i = 1, 2, 3) \tag{36}
$$

where l_i is the length of the i-th actuator in an undeformed configuration.

3.3. Geographically distributed testing

As described above, the coordination procedure involves iterative exchange of displacement feedback and force commands, ensuring compatibility and equilibrium at the interface.

To implement this coupling in a flexible and scalable way, a distributed software architecture was adopted.

The principle behind the design of the developed geographically distributed testing framework is to link computational and experimental facilities through the internet while preventing stakeholders from disclosing critical information on the computational model and experimental specimens. Therefore, the distributed software architecture reported in Figure 8 was adopted. The network relies on three building blocks:

- *Numerical substructure node*: In the presented application, this node is physically located at Aarhus University, Denmark. The related code is implemented as a Python script. At each time step of the HT procedure:

  1. It fetches the PS interface displacements (θ_x and θ_y) in TASK-SPACE from the messaging system.
  2. It solves the hybrid model equation of motion and simulates the NS.
  3. It posts the NS interface forces (λ_1 and λ_2) and pitch displacement (β) in TASK-SPACE to the messaging system.

- *Physical Interface node*: In the presented application, this node is physically located at the laboratory of FORCE TECHNOLOGY, Denmark. The related code is implemented as a Python script. At each time step of the HT procedure:

  1. It fetches the NS interface forces (λ_1 and λ_2) and pitch displacement (β) in TASK-SPACE from the messaging system.
  2. It converts interface forces and displacement from TASK-SPACE to JOINT-SPACE.
  3. It sends JOINT-SPACE forces/displacements (τ_1, τ_2 and q_3) to the MTS control system via EtherCAT.
  4. It receives the corresponding JOINT-SPACE displacement (q_1 and q_2)
  5. It converts JOINT-SPACE displacement/forces to TASK-SPACE
  6. It posts TASK-SPACE displacement/forces (θ_x and θ_y) to the messaging system.

- *messaging system*: cloud-based messaging broker implemented using *Azure Event Hub*, a distributed event streaming platform designed for high-throughput, low-latency data exchange [41]. At each time step of the HT procedure:

  – It dispatches messages received from the *simulation node* to the network.
  – It dispatches messages received from the *testing node* to the network.
  – It performs data logging.

The cyclic exchange of messages between *numerical substructure node* and *physical interface node* within step of the HT procedure is graphically depicted in the sequence diagram of Figure 9. In the presented application, numerical integration was performed with a time

step of 10 ms, while actuator setpoints were updated with an average rate of ≈ 0.3 Hz to ensure quasi-static conditions on the test bench.

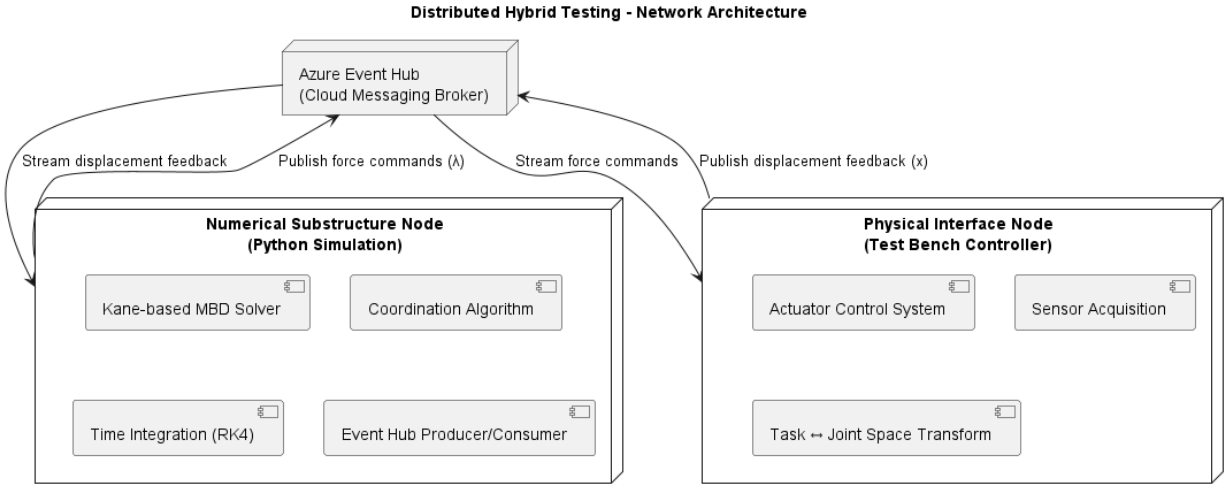

Figure 8: Network architecture for geographically distributed HT: the *numerical substructure node* and the *physical interface node* exchange force commands and displacement feedback through the *messaging system*.

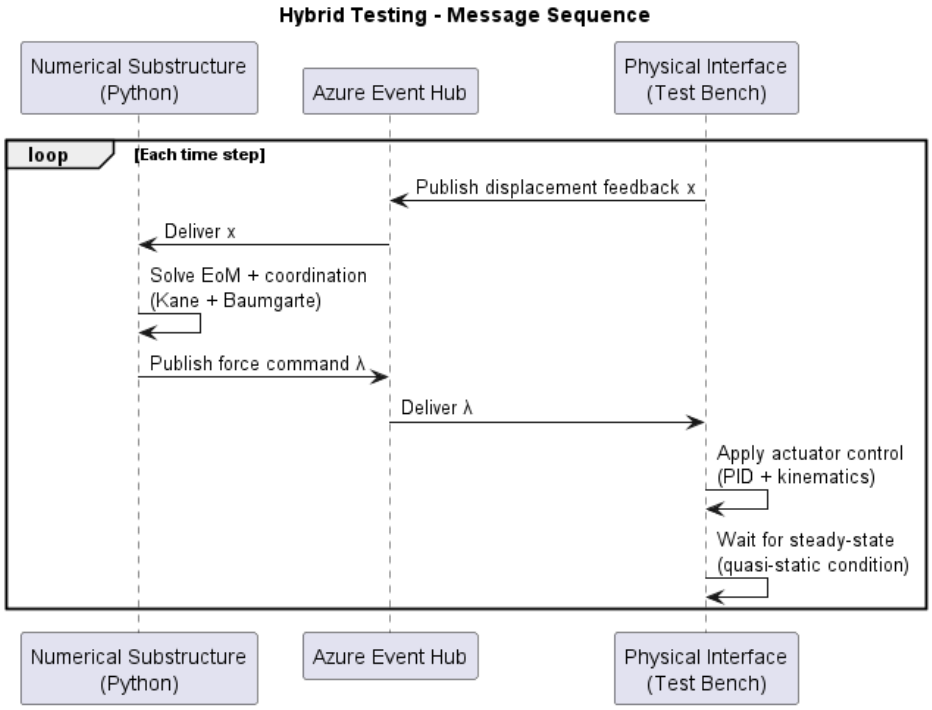

Figure 9: Message sequence for one HT time step, showing how displacement feedback is published from the physical interface node, processed by the numerical substructure node, and returned as force commands through Azure Event Hub.

A key feature of this implementation is that communication is *asynchronous*, but the algorithm behaves *synchronously* at the logical level by enforcing a stepwise loop. Both

simulation and testing nodes interact only via message streams; therefore, they can be easily verified independently. Additional components, such as data logging and monitoring services, can be attached to the message stream without affecting the other components. Temporary disconnections do not cause the HT to fail since messages are buffered.

4. Results and discussion

4.1. Validation of the framework

Before executing the HT, the formulation and coordination algorithm are validated using a fully numerical replica of the hybrid model. This validation assesses both the correctness of the hybrid model formulation and the numerical stability of the coordination algorithm. In the numerical validation of the hybrid model, the PS pitch bearing is replaced by a virtual counterpart (vPS) with approximated mechanical properties. The first three steps of the coordination scheme shown in Figure 6 are retained. The fourth step, which normally involves the experimental response of the PS, is instead performed numerically by transforming the actuator forces into bending moments in the pitch bearing using (31). Based on an estimated bearing flexibility, the bending angles θ_x^{vfbk} and θ_y^{vfbk} are computed and provided as virtual feedback (vfbk). The vPS response is then transformed into actuator elongations via (29) and returned to the hybrid model.

The numerical validation, referred to as the virtual hybrid test (vHT), is compared against a conventional numerical simulation (sim). The results for the vPS are shown in Figure 10, while the responses of all components in the NS are presented in Figure 11.

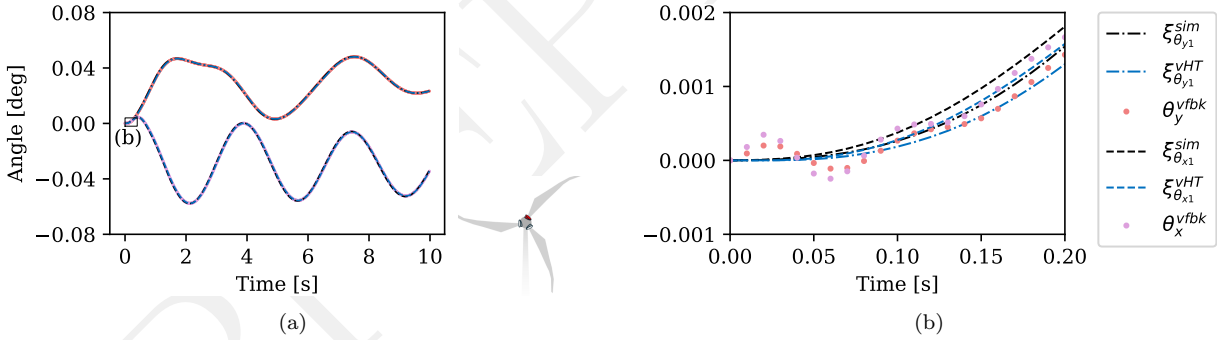

Figure 10: Validation results for pitch bearing 1, which here is a virtual physical substructure. a) shows the full dataset, and b) is zoomed in on the first 0.2 s

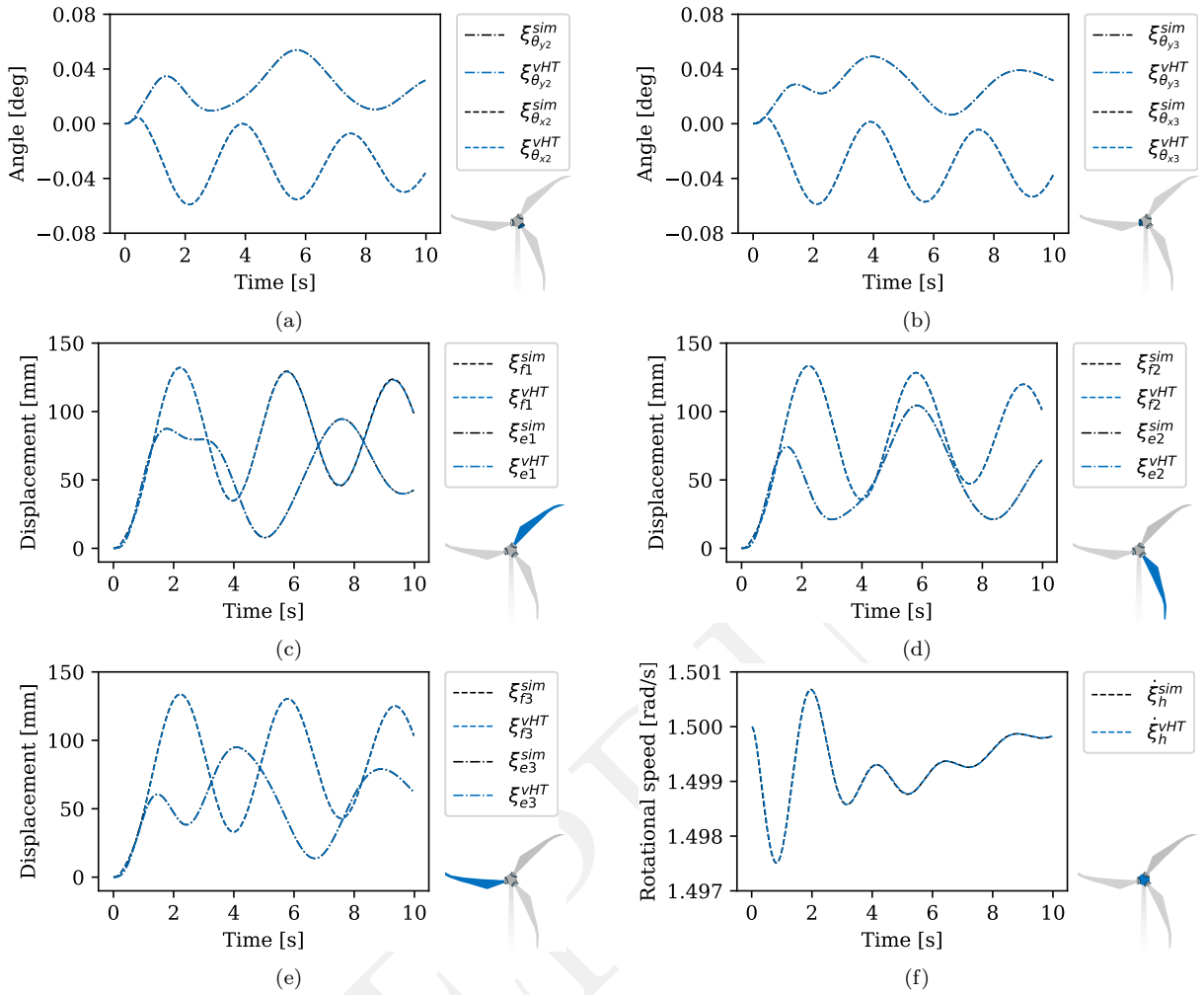

Figure 11: Validation results for a) pitch bearing 2 and b) pitch bearing 3, c) blade 1, d) blade 2, e) blade 3, and f) hub. The presented results are all for numerical substructures

The behavior of the hybrid test is quantified using performance indices adapted from the hybrid testing criteria proposed by Silva et al. [9]. The hybrid test response for each degree-of-freedom j is compared to the reference simulation with,

$$J_{1,j} = \sqrt{\frac{\sum_{k=1}^{N}[\xi_j(t_k) - \xi_j^{sim}(t_k)]^2}{\sum_{k=1}^{N}[\xi_j^{sim}(t_k)]^2}} \times 100\% \tag{37}$$

and displacement compatibility mismatch between the NS and PS is quantified by,

$$J_{2,j} = \sqrt{\frac{\sum_{k=1}^{N}[\theta_j(t_k) - \xi_{\theta_j}(t_k)]^2}{\sum_{k=1}^{N}[\xi_{\theta_j}(t_k)]^2}} \times 100\% \tag{38}$$

For the virtual hybrid test, the performance metrics are presented in Table 1 and 2.

Table 1: Reference simulation mismatch quantifiers for the virtual hybrid test

		$\xi_{\theta_{xi}}$	$\xi_{\theta_{yi}}$	ξ_{ei}	ξ_{fi}
$J_{1,j}$ [%]	Blade 1	2.19	1.36	0.49	0.57
	Blade 2	0.93	0.76	0.78	0.63
	Blade 3	0.97	0.51	0.56	0.66

Table 2: Displacement compatibility quantifiers for the virtual hybrid test

	θ_x	θ_y
$J_{2,j}$ [%]	0.51	0.33

The numerical replica of the hybrid model produces responses close to those of the conventional numerical simulation for both the vPS in Figure 10 and the NS in Figure 11. This agreement is supported by the error metrics in Table 1, where all reference simulation mismatches remain below 2.2%. The largest deviations occur for the bending coordinates of blade 1, which are directly coupled to the vPS, while the remaining DOFs show errors close to or below 1%. This indicates that the hybrid formulation and coordination introduces only minor deviations into the system response.

The displacement compatibility errors in Table 2 are 0.51% for θ_x and 0.33% for θ_y, showing that the coordination algorithm enforces the interface constraint with small mismatch. The small oscillations observed in Figure 10 are therefore not associated with a significant loss of compatibility or accuracy. They are attributed to irregularities in the displacement feedback and are mitigated through Baumgarte stabilization.

The choice of Baumgarte stabilization parameters plays a crucial role in this regard: while reducing the parameters slightly attenuates the oscillations, it also increases the simulation's sensitivity to noise, potentially leading to instability. In the vHT, the Baumgarte stabilization parameters are manually calibrated to $\alpha = \beta = 7$, and these values are subsequently used in the physical hybrid test.

4.2. Hybrid testing results

The HT results for the WT rotor system are presented in Figure 12 for the PS pitch bearing. The results for the remaining NS components are shown in Figure 13.

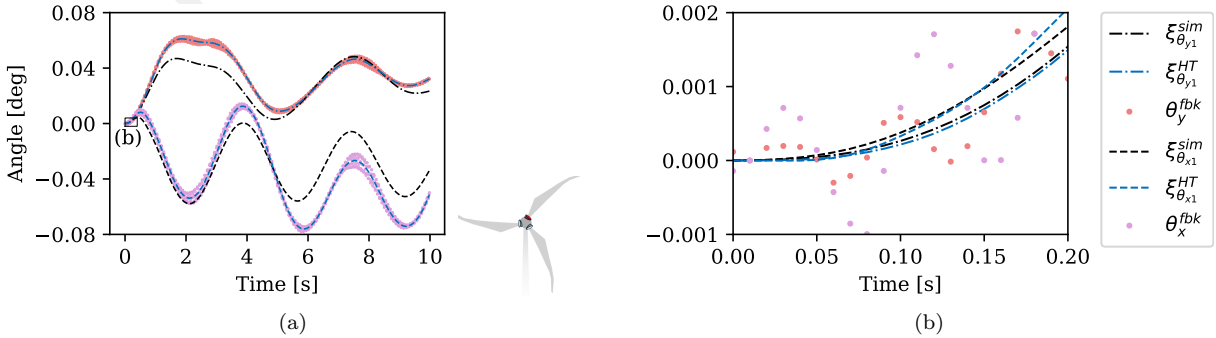

Figure 12: Hybrid test results for pitch bearing 1, which here is a physical substructure. a) shows the full dataset, while b) presents a close-up of the first 0.2 s

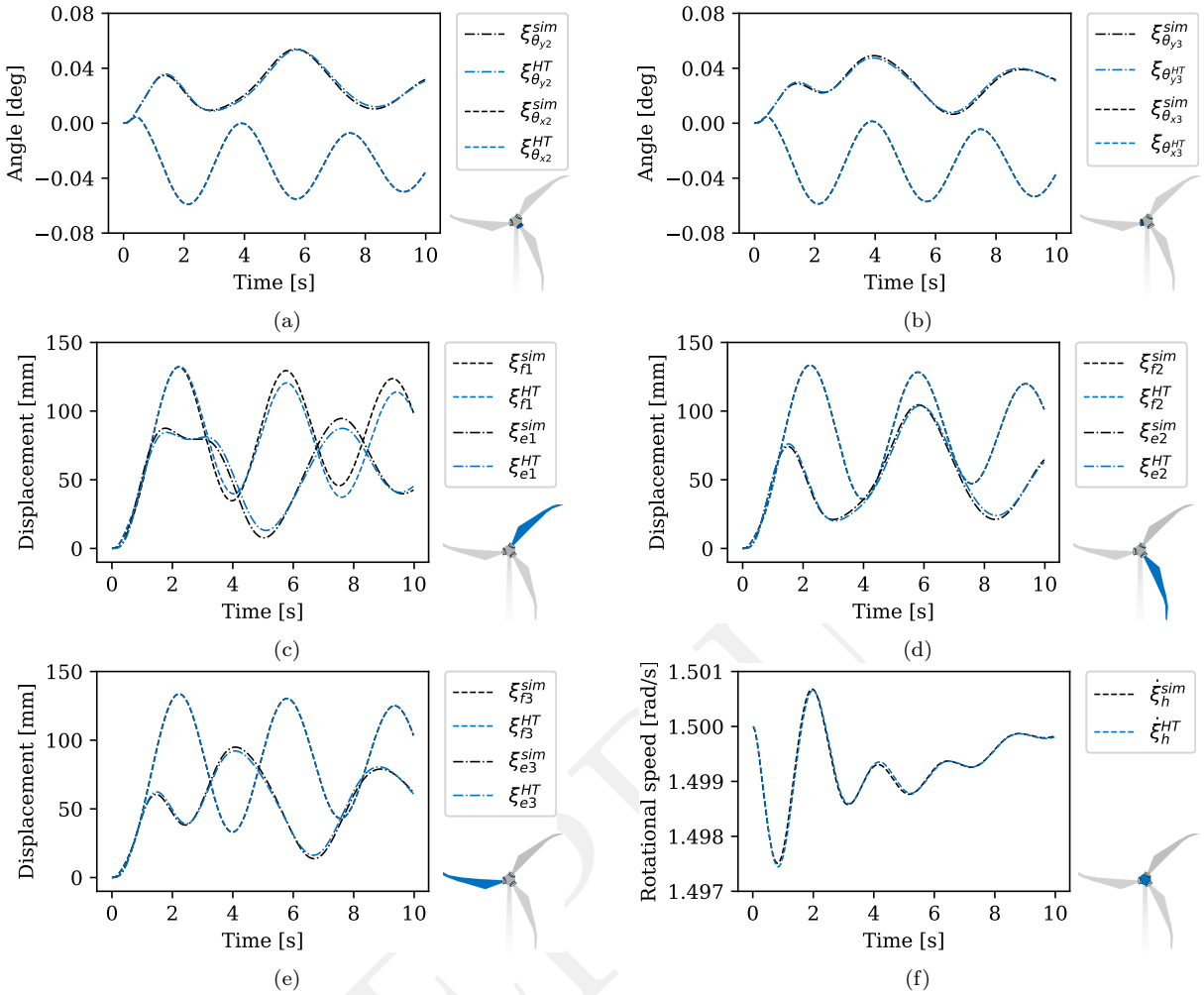

Figure 13: Hybrid test results for a) pitch bearing 2 and b) pitch bearing 3, c) blade 1, d) blade 2, e) blade 3, and f) hub. The presented results are all for numerical substructures

The reference simulation mismatch from (37) and displacement compatibility mismatch from (38) are quantified in Tables 3 and 4, respectively.

Table 3: Reference simulation mismatch quantifiers for the hybrid test

		$\xi_{\theta_{xi}}$	$\xi_{\theta_{yi}}$	ξ_{ei}	ξ_{fi}
$J_{1,j}$ [%]	Blade 1	44.57	28.11	6.87	8.53
	Blade 2	0.86	4.85	4.27	0.59
	Blade 3	0.88	3.95	3.48	0.61

Table 4: Displacement compatibility mismatch quantifiers for the hybrid test

	θ_x	θ_y
$J_{2,j}$ [%]	4.79	2.59

The mismatch metrics show that the physical pitch bearing behaves differently from its numerical counterpart. In Table 3, the largest errors occur for blade 1, with $J_{1,j} = 44.57\%$ for $\xi_{\theta_{x1}}$ and 28.11% for $\xi_{\theta_{y1}}$. This is expected, since blade 1 is directly coupled to the PS. The reference simulation uses an approximate linear bearing stiffness, whereas the physical bearing includes nonlinear effects that are not captured by the numerical bearing model. The errors therefore reflect the difference between the assumed numerical bearing stiffness and the actual experimental response.

This difference also affects the rest of the rotor. For blade 1, the blade-tip displacement errors reach 6.87% and 8.53%, while the indirectly coupled blades show errors up to 4.85%. This demonstrates the main motivation for HT: a change in the physical component response changes the motion of the full structure, which cannot be captured by the reference simulation alone.

The displacement compatibility errors in Table 4 are 4.79% for θ_x and 2.59% for θ_y. These values are higher than in the vHT, mainly due to noise in the displacement feedback and inaccuracies in the experimental setup. Despite this, the PS motion in Figure 12 remains smooth and the HT remains stable. This is important for force-controlled HT, which is generally sensitive to feedback noise. The result shows that the Baumgarte stabilization reduces the sensitivity to noisy feedback while maintaining stable coupling between the NS and PS.

The exchange of command and feedback signals in the experimental setup is illustrated in Figure 14.

The geometric transformation between task-space and joint-space coordinates demonstrates satisfactory performance. A linear relationship is maintained between bending moments and angles in the task-space domain for small pitching motions. However, for larger pitch rotations, as shown in Figure 14b, the hysteresis plot in Figure 14h reveals a notable nonlinearity. This nonlinearity likely results from the simplified straight-pipe assumption, which does not fully capture the small displacements introduced by rotational deformation and distorts the results.

Overall, the WT rotor motion in the HT follows the trends observed in the numerical simulation, confirming a successful implementation of the interface forces in the hybrid model and demonstrating the stability of the coordination algorithm.

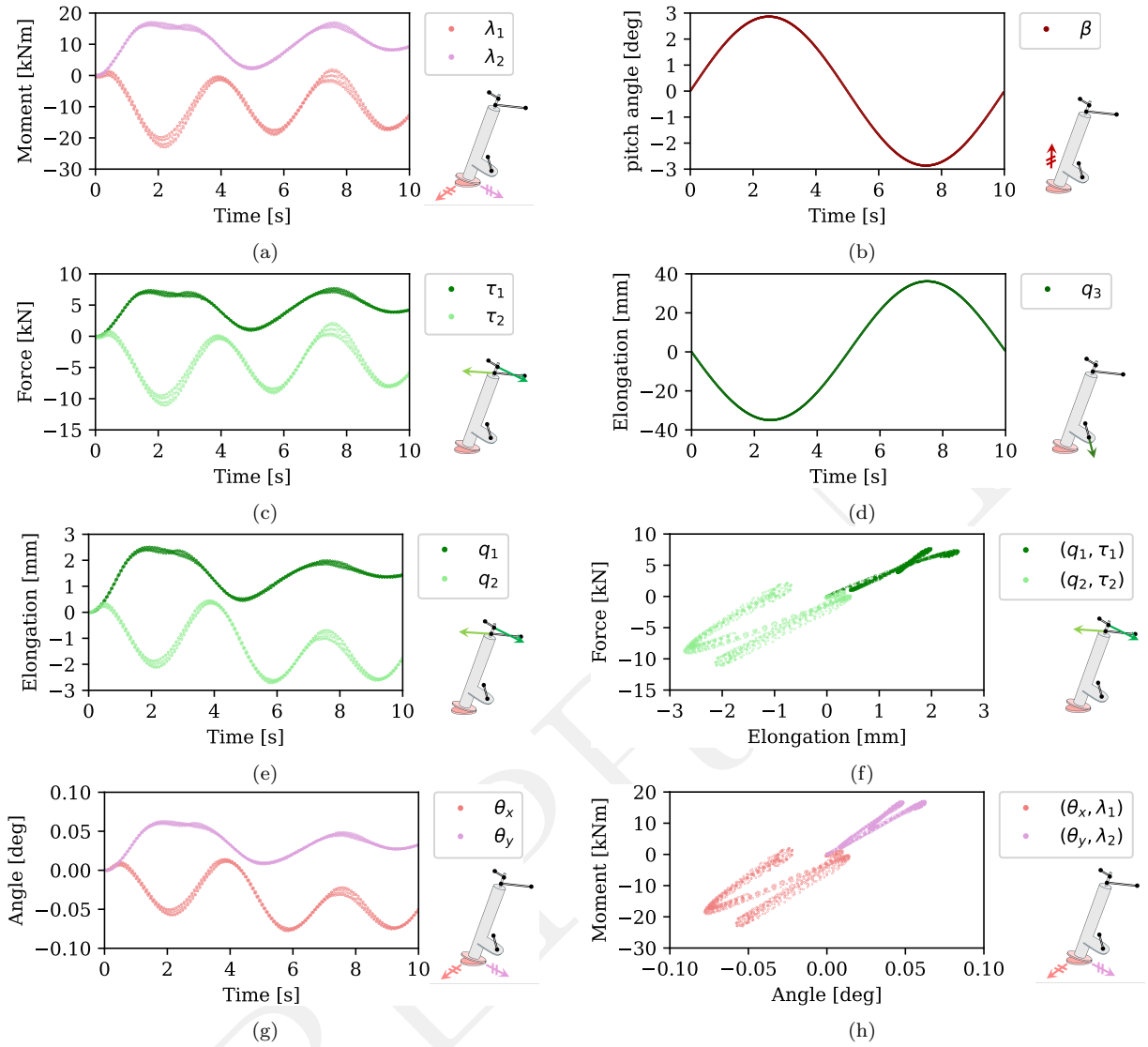

Figure 14: Experimental hybrid testing results showing: a) bending moment commands, b) pitch angle command, c) actuator force commands, d) pitch actuator elongation, e) actuator elongation feedback, f) actuation hysteresis, g) pitch bearing bending angle feedback, and h) pitch bearing bending angle hysteresis

5. Conclusion

This work has presented a hybrid testing framework for multibody dynamic systems, tailored to wind turbine mechanical components. The equations of motion are derived using Kane's method, and interface forces are introduced through the principle of virtual power. The framework supports mixed-mode control, with task-space and joint-space coupling formulated using robotic kinematics.

The framework is demonstrated on a 13-degree-of-freedom simplified wind turbine rotor model, where one pitch bearing is tested as the physical substructure. A virtual hybrid test validates the formulation and coordination algorithm, with all reference simulation mismatches below 2.2% and displacement compatibility errors of 0.51% and 0.33%.

The physical hybrid test shows that the pitch bearing differs from its numerical counterpart. This leads to large mismatches for the directly coupled blade, with $J_{1,j} = 44.57\%$ and 28.11% for the two pitch-bearing bending coordinates. The difference also propagates to the remaining rotor DOFs, showing that changes in the physical substructure response can modify the motion of the full structure.

Despite displacement feedback noise and force-controlled bending, the hybrid test remains stable. The displacement compatibility errors are limited to 4.79% and 2.59%, indicating that Baumgarte stabilization reduces sensitivity to noisy feedback while maintaining stable coupling between the NS and PS.

The experiments are performed in a pseudo-dynamic regime. Extension to real-time hybrid testing, including the coupled dynamics of the PS and transfer system, will be addressed in future work.

CRediT authorship contribution statement

F. Nordtorp: Writing – review & editing, Writing – original draft, Visualization, Investigation, Formal analysis, Validation, Software, Methodology. **E. E. Baş**: Writing – review & editing, Project administration, Investigation, Software, Methodology, Conceptualization. **C. Gomes**: Writing – review & editing, Investigation, Software, Methodology, Conceptualization. **P. Jensen**: Writing – review & editing, Resources, Investigation, Methodology. **J. Jørgensen**: Writing – review & editing, Resources, Investigation, Methodology. **G. Abbiati**: Writing – review & editing, Project administration, Supervision, Methodology, Conceptualization.

Declaration of competing interest

The authors declare that they have no known competing financial interests or personal relationships that could have appeared to influence the work reported in this paper.

Acknowledgements

This research was funded by EUDP – the Energy Technology Development and Demonstration Program – through the following projects:

- Project 64019-0595 DLTE, a collaboration between Aarhus University, Department of Electrical and Computer Engineering and Department of Civil and Architectural Engineering (AU-ECE, AU-CAE), R&D Test Systems A/S, and FORCE Technology.
- Project 640222-497272 DIGIT-BENCH, a collaboration between Aarhus University, Department of Electrical and Computer Engineering and Department of Civil and Architectural Engineering (AU-ECE, AU-CAE), R&D Test Systems A/S, and Lindø Offshore Renewable Center (LORC).

Data Availability Statement

Some or all data, models, or code that support the findings of this study are available from the corresponding author upon reasonable request.

References

[1] M. Hakuno, M. Shidawara, and T. Hara, "Dynamic destructive test of a cantilever beam, controlled by an analog computer," 1969.

[2] K. Takanashi, K. Udagawa, M. Seki, T. Okada, and H. Tanaka, "Non-linear earthquake response analysis of structures by a computer-actuator on-line system," *Transaction of the Architectural Institute of Japan*, vol. 229, pp. 77–83, 03 1975.

[3] P. Pan, T. Wang, and M. Nakashima, *Development of online hybrid testing: theory and applications to structural engineering*. Oxford [England] ; Waltham, MA: Elsevier / Butterworth Heinemann, 2016.

[4] V. Saouma and M. Sivaselvan, *Hybrid simulation: Theory, implementation and applications*. CRC Press, 2014.

[5] A. Sauca, N. Mortensen, A. Drustrup, and G. Abbiati, "Experimental validation of a hybrid fire testing framework based on dynamic relaxation," *Fire Safety Journal*, vol. 121, p. 103315, 2021.

[6] C. Neumann *et al.*, "Hydrodynamic real-time hybrid simulation demonstrated for wave–structure interaction," *Journal of Waterway, Port, Coastal, and Ocean Engineering*, 2023.

[7] W. Su and W. Song, "A real-time hybrid aeroelastic simulation platform for flexible wings," *Aerospace Science and Technology*, vol. 95, p. 105513, 2019.

[8] G. Fermandois and B. F. Spencer, "Model-based framework for multi-axial real-time hybrid simulation testing," *Earthquake Engineering and Engineering Vibration*, vol. 16, no. 4, pp. 671–691, 2017.

[9] C. E. Silva, D. Gomez, A. Maghareh, S. J. Dyke, and B. F. Spencer, "Benchmark control problem for real-time hybrid simulation," *Mechanical Systems and Signal Processing*, vol. 135, p. 106381, 2020.

[10] G. Abbiati, O. S. Bursi, P. Caperan, L. Di Sarno, F. J. Molina, F. Paolacci, and P. Pegon, "Hybrid simulation of a multi-span rc viaduct with plain bars and sliding bearings," *Earthquake Engineering & Structural Dynamics*, vol. 44, no. 13, pp. 2221–2240, 2015.

[11] T. Sauder, V. Chabaud, M. Thys, E. E. Bachynski, and L. O. Sæther, "Real-Time Hybrid Model Testing of a Braceless Semi-Submersible Wind Turbine: Part I — The Hybrid Approach," in *Volume 6: Ocean Space Utilization; Ocean Renewable Energy*, (Busan, South Korea), p. V006T09A039, American Society of Mechanical Engineers, June 2016. 34 citations (Crossref) [2023-08-31].

[12] M. Belloli, I. Bayati, A. Facchinetti, A. Fontanella, H. Giberti, F. La Mura, F. Taruffi, and A. Zasso, "A hybrid methodology for wind tunnel testing of floating offshore wind turbines," *Ocean Engineering*, vol. 210, p. 107592, 2020.

[13] Z. Zhang, A. Staino, B. Basu, and S. R. Nielsen, "Performance evaluation of full-scale tuned liquid dampers (tlds) for vibration control of large wind turbines using real-time hybrid testing," *Engineering Structures*, vol. 126, pp. 417–431, 2016.

[14] S. Herrmann, M. Kaehler, R. Souffrant, R. Rachholz, J. Zierath, D. Kluess, W. Mittelmeier, C. Woernle, and R. Bader, "Hil simulation in biomechanics: A new approach for testing total joint replacements," *Computer Methods and Programs in Biomedicine*, vol. 105, no. 2, pp. 109–119, 2012.

[15] P. Shao, W. Guo, Q. Lei, and C. Zeng, "Adaptive compound control for the real-time hybrid simulation of high-speed railway train–bridge coupling vibration," *Structural Control and Health Monitoring*, vol. 28, 07 2021.

[16] W. Guo, C. Zeng, H. Gou, Q. Gu, T. Wang, H. Zhou, B. Zhang, and J. Wu, "Real-time hybrid simulation of high-speed train-track-bridge interactions using the moving load convolution integral method," *Engineering Structures*, vol. 228, p. 111537, 2021.

[17] H. Liu, Z. Tang, and R. Enokida, "Stability prediction method of time-varying real-time hybrid testing system on vehicle-bridge coupled system," *Mechanical Systems and Signal Processing*, vol. 216, p. 111463, 2024.

[18] W. Witteveen and L. Koller, "Frf-based non-simultaneous real-time hybrid testing of multiple subsystems with moderate nonlinearities," *Mechanical Systems and Signal Processing*, vol. 188, p. 109944, 2023.

[19] F. Aghili and J.-C. Piedboeaeuf, "Emulation of robots interacting with environment," *Mechatronics, IEEE/ASME Transactions on*, vol. 11, pp. 35 – 46, 03 2006.

[20] J. Jonkman, M. Sprague, and colleagues of NREL, "OpenFAST — wind research — NREL," 2024. Accessed: 2024-01-02.

[21] S. Sarkar and B. Fitzgerald, "Use of kane's method for multi-body dynamic modelling and control of spar-type floating offshore wind turbines," *Energies*, vol. 14, p. 6635, 10 2021.

[22] T. Kane and C. Wang, "On the derivation of equations of motion," *Journal of the Society of Industrial and Applied Mechanics*, vol. 13, no. 2, pp. 487–492, 1965.

[23] T. Kane and D. Levinson, "Formulation of equations of motion for complex spacecraft," *Journal of Guidance, Control, and Dynamics*, vol. 3, no. 2, pp. 99–112, 1980.

[24] A. Banerjee, *Flexible Multibody Dynamics: Efficient Formulations with Applications*. CRC Press, 2nd ed., 2022.

[25] C. Roithmayr and D. H. Hodges, *Dynamics: Theory and Application of Kane's Method*. Cambridge University Press, 2016.

[26] J. K. Moore, "Learn multibody dynamics," 2022.

[27] SymPy Development Team, "Sympy documentation," 2023. Accessed on January 16, 2024.

[28] F. Nordtorp, E. E. Baş, C. Gomes, and G. Abbiati, "A hybrid testing framework for wind turbine mechanical components," *Journal of Physics: Conference Series*, vol. 2767, p. 052046, jun 2024.

[29] M. Géradin and A. Cardona, *Flexible Multibody Dynamics: A Finite Element Approach*, vol. 4. 01 2001.

[30] F. Nordtorp and G. Abbiati, "A dae solver for coordination of force-controlled hybrid testing," 2026. engrXiv preprint.

[31] U. M. Ascher and L. R. Petzold, *Computer Methods for Ordinary Differential Equations and Differential-Algebraic Equations*. USA: Society for Industrial and Applied Mathematics, 1st ed., 1998.

[32] T. N. Santelo, C. M. R. de Oliveira, C. D. Maciel, and J. R. B. de A. Monteiro, "Wind turbine failures review and trends," vol. 33, no. 2, pp. 505–521.

[33] F. IWES, *Pitch Bearing Testing at IWES*. Available at https://www.iwes.fraunhofer.de/en/test-centers-and-measurements/drive-train-components.html2, accessed: 24.11.2022.

[34] F. IWES, *Fraunhofer IWES puts further bearing test rig into operation*. Available at https://www.iwes.fraunhofer.de/en/press/archive-2021/fraunhofer-iwes-puts-further-bearing-test-rig-into-operation.html, accessed: 24.11.2022.

[35] J. Han, J. Nam, Y. Park, G. Lee, and Y. Nam, "An experimental study on the performance and fatigue life of pitch bearing for wind turbine," *Journal of Mechanical Science and Technology*, vol. 29, pp. 1963–1971, 05 2015.

[36] F. IWES, *Pitch Bearing Testing at IWES*. Available at https://www.iwes.fraunhofer.de/de/download-center/pitch-bearing-testing-at-iwes.html, accessed: 24.11.2022.

[37] IDOM, *Windturbine Blade Bearings Test Bench*. Available at https://www.idom.com/en/project/windturbine-blade-bearings-test-bench/, accessed: 24.11.2022.

[38] L. WindPower, *Construction Underway on Largest Wind Turbine Rotor Test Rig at Netherlands Technology Center*. Available at tinyurl.com/4uvcnrpy, accessed: 24.11.2022.

[39] M. Stammler, P. Thomas, A. Reuter, F. Schwack, and G. Poll, "Effect of load reduction mechanisms on loads and blade bearing movements of wind turbines," *Wind Energy*, vol. 23, pp. 274–290, 2020.

[40] H. Taghirad, *Parallel robots mechanics and control*. 2013.

[41] Microsoft, "What is Azure Event Hubs?." https://learn.microsoft.com/en-us/azure/event-hubs/event-hubs-about. Microsoft Learn. Last updated: 28 January 2026. Accessed: 4 May 2026.

Appendix A. Full derivation

The parameters describing the model are defined in Table A.5.

Table A.5: Model parameters for the simplified wind turbine rotor system.

Description	Symbol	Value	Unit
Blade length	l_b	35	m
Blade mass 1	m_{b1}	7000	kg
Blade mass 2	m_{b2}	5000	kg
Blade mass 3	m_{b3}	3000	kg
Blade damping	c_b	840	kNs/m
Blade stiffness	k_b	15.45	kN/m
Pitch bearing stiffness	k_p	21000	kNm
Applied load x-direction	f_x	525	kN
Applied load y-direction	f_y	105	kN
Geartrain mass of inertia	I_g	$2.0 \cdot 10^6$	kgm^2
Geartrain damping	c_g	21	$kNms$
Gravity	g	9.82	m/s^2
Ramping time instance	t_0	0.5	s
Ramping parameter	γ	$2.8 \cdot 10^{-3}$	-

(i) The hub frame B_0 is oriented with ξ_0 in the $\hat{\mathbf{n}}_y$-direction,

$$ {}^{N}\mathbf{C}^{B_0} = \begin{bmatrix} \cos(\xi_0) & 0 & \sin(\xi_0) \\ 0 & 1 & 0 \\ -\sin(\xi_0) & 0 & \cos(\xi_0) \end{bmatrix} \tag{A.1} $$

Between blade frame B_i and frame N, a frame A_i is attached to each pitch bearing.

$$ {}^{N}\mathbf{C}^{A_i} = \begin{bmatrix} -\sin(\xi_0+\Psi_i)\cos(\beta) & \sin(\xi_0+\Psi_i)\sin(\beta) & \cos(\xi_0+\Psi_i) \\ \sin(\beta) & \cos(\beta) & 0 \\ -\cos(\xi_0+\Psi_i) & \cos(\xi_0+\Psi_i)\sin(\beta) & -\sin(\xi_0+\Psi_i) \end{bmatrix}, \quad (i=1,2,3) \tag{A.2} $$

where $\Psi_1 = 0$, $\Psi_2 = 2\pi/3$ and $\Psi_3 = 4\pi/3$ are the initial azimuth angles of the three blades.

$$ {}^{A_i}\mathbf{C}^{B_i} = \begin{bmatrix} \cos(\xi_{\theta_{yi}}) & \sin(\xi_{\theta_{xi}})\sin(\xi_{\theta_{yi}}) & \cos(\xi_{\theta_{xi}})\sin(\xi_{\theta_{yi}}) \\ 0 & \cos(\xi_{\theta_{xi}}) & -\sin(\xi_{\theta_{xi}}) \\ -\sin(\xi_{\theta_{yi}}) & \sin(\xi_{\theta_{xi}})\cos(\xi_{\theta_{yi}}) & \cos(\xi_{\theta_{xi}})\cos(\xi_{\theta_{yi}}) \end{bmatrix}, \quad (i=1,2,3) \tag{A.3} $$

(ii) Relative positions of nodes

$$\mathbf{p}^{OP_{i0}} = l_3\hat{\mathbf{b}}_{iz}, \quad (i = 1, 2, 3) \tag{A.4}$$

$$\mathbf{p}^{OP_{ik}} = l_k\hat{\mathbf{b}}_{iz} + \phi(l_k)\xi_{fi}\hat{\mathbf{b}}_{iy} + \phi(l_k)\xi_{ei}\hat{\mathbf{b}}_{ix}, \quad (i = 1, 2, 3)\ (k = 1, 2, 3) \tag{A.5}$$

$$\phi(z) = \frac{z^2(3l_3 - z)}{2l_3^3} \tag{A.6}$$

(iii) Inertia forces and torques

$$\mathbf{f}^{*P_{ik}} = -m_k\,{}^N\mathbf{a}^{P_{ik}}, \quad (i = 1, 2, 3)\ (k = 1, 2, 3) \tag{A.7}$$

$$\mathbf{t}^{*B_i} = -\mathbf{I}^{B_i} \cdot {}^N\boldsymbol{\alpha}^{B_i} - {}^N\boldsymbol{\omega}^{B_i} \times \left(\mathbf{I}^{B_i} \cdot {}^N\boldsymbol{\omega}^{B_i}\right), \quad (i = 0, 1, 2, 3) \tag{A.8}$$

$$\mathbf{I}^{B_0} = I_g\hat{\mathbf{b}}_{0y} \otimes \hat{\mathbf{b}}_{0y}, \quad \mathbf{I}^{B_i} = I_b\hat{\mathbf{b}}_{iz} \otimes \hat{\mathbf{b}}_{iz}, \quad (i = 1, 2, 3) \tag{A.9}$$

(iv) Active forces and torques

$$\mathbf{f}^{P_{ik}} = \Gamma(t)\left(-m_k g\hat{\mathbf{n}}_z + f_{xk}\hat{\mathbf{b}}_{ix} + f_{yk}\hat{\mathbf{b}}_{iy}\right), \quad (i = 1, 2, 3)\ (k = 1, 2, 3) \tag{A.10}$$

$$\mathbf{f}^{P_{i3}} = \mathbf{f}^{P_{i3}} + (-k_b\xi_{ei} - c_b\dot{\xi}_{ei})\hat{\mathbf{b}}_{ix} + (-k_b\xi_{fi} - c_b\dot{\xi}_{fi})\hat{\mathbf{b}}_{iy}, \quad (i = 1, 2, 3) \tag{A.11}$$

$$\mathbf{f}^{P_{i0}} = (k_b\xi_{ei} + c_b\dot{\xi}_{ei})\hat{\mathbf{b}}_{ix} + (k_b\xi_{fi} + c_b\dot{\xi}_{fi})\hat{\mathbf{b}}_{iy}, \quad (i = 1, 2, 3) \tag{A.12}$$

$$\mathbf{t}^{B_0} = -c_g\dot{\xi}_h\hat{\mathbf{n}}_y \tag{A.13}$$

$$\mathbf{t}^{A_i} = k_p\xi_{\theta_{xi}}\hat{\mathbf{a}}_{ix} + k_p\xi_{\theta_{yi}}\hat{\mathbf{a}}_{iy}, \quad (i = 2, 3) \tag{A.14}$$

$$\mathbf{t}^{B_i} = -k_p\xi_{\theta_{xi}}\hat{\mathbf{a}}_{ix} - k_p\xi_{\theta_{yi}}\hat{\mathbf{a}}_{iy}, \quad (i = 2, 3) \tag{A.15}$$

(v) Interface forces and torques

$$\mathbf{t}^{\lambda A_1} = \lambda_1\hat{\mathbf{a}}_{1x} + \lambda_2\hat{\mathbf{a}}_{1y} \tag{A.16}$$

$$\mathbf{t}^{\lambda B_1} = -\lambda_1\hat{\mathbf{a}}_{1x} - \lambda_2\hat{\mathbf{a}}_{1y} \tag{A.17}$$

(vi) Kane method

$$
\begin{aligned}
F_j = \sum_{i=1}^{3} {}^N\mathbf{v}_j^{P_{i0}} \cdot \mathbf{f}^{P_{i0}} + \sum_{i=1}^{3}\sum_{k=1}^{3} {}^N\mathbf{v}_j^{P_{ik}} \cdot (\mathbf{f}^{*P_{ik}} + \mathbf{f}^{P_{ik}}) \\
+ {}^N\boldsymbol{\omega}_j^{B_0} \cdot (\mathbf{t}^{*B_0} + \mathbf{t}^{B_0}) + \sum_{i=1}^{3} {}^N\boldsymbol{\omega}_j^{A_i} \cdot \mathbf{t}^{A_i} + \sum_{i=1}^{3} {}^N\boldsymbol{\omega}_j^{B_i} \cdot (\mathbf{t}^{*B_i} + \mathbf{t}^{B_i}) \\
+ {}^N\boldsymbol{\omega}_j^{A_1} \cdot \mathbf{t}^{\lambda A_1} + {}^N\boldsymbol{\omega}_j^{B_1} \cdot \mathbf{t}^{\lambda B_1}, \quad (j = 1, 2, \ldots, 13)
\end{aligned}
\tag{A.18}
$$